ELSEVIER





# Self-powered bimodal tactile imaging device for ultrasensitive pressure sensing, real-time visualization recognition, and intelligent control

**Kangting Liu [a], Yifan Xia [a], Xinrong Zhi [a], Shuhan Li [a], Siyu Zhang [a], Biao Yang [a], Mingyuan Li [a], Xin Wang [a,b,*], Caofeng Pan [c,*]**

[a] Henan Key Laboratory of Quantum Materials and Quantum Energy, School of Future Technology, Henan University, Kaifeng 475004, PR China
[b] School of Information and Artificial Intelligence, Anhui Agricultural University, Hefei 230036, PR China
[c] Institute of Atomic Manufacturing, Beihang University, Beijing 100191, PR China

**In the domain of smart robotics, the refinement of tactile imaging constitutes a seminal element for enhancement of human–machine interaction (HMI) and enrichment of artificial intelligence (AI). This field is confronted with dual challenges of achieving high-sensitive pressure detection and precise localization of tactile stimuli. In response, the current research introduces a groundbreaking self-powered bimodal tactile imaging device (TID), featuring a configuration of high-dielectric thin film superimposed on laser-induced graphene (LIG) electrodes. This pioneering design is conceived to facilitate not only the detection of subtle pressure but also to support real-time visual recognition and intelligent control functionalities. The bimodal nature of the TID allows for the transformation of slight tactile inputs into both luminous triboelectrification-induced electroluminescence (TIEL) and measurable electrical signals, thereby seamlessly merging the realms of tactile perception and optical display. Leveraging the luminosity of TIEL, the TID adeptly achieves tactile imaging and immediate visual recognition, with its capabilities further enhanced through the integration of machine learning algorithms. Additionally, the TID exhibits a remarkable proficiency in precise tactile localization, through the analysis of voltage outputs initiated by delicate touching and sliding motions. Moreover, an advanced intelligent control system, predicated on the optical-electrical dual-modal sensing provided by the TID, has been developed. This system illustrates the synergistic fusion of visual recognition with accurate tactile localization, underscoring the substantial utility of the bimodal TID across diverse applications in HMI, AI, and intelligent robotic platforms and heralding new avenues for interactive and responsive robotic systems.**

**Keywords: Ultrasensitive pressure sensing; Triboelectrification-induced electroluminescence; Bimodal tactile imaging; Real-time visualization recognition; Intelligent control; Self-powered**

## Introduction

In engaging with the dynamic and complex real world, humans can process adeptly multiple sensory inputs through an adaptive, plastic, and event-driven neural network, allowing for an accurate representation of the environment [1]. The emulation of such biological sensor-based functionality could fundamentally

* Corresponding authors at: School of Information and Artificial Intelligence, Anhui Agricultural University, Hefei 230036, PR China and School of Future Technology, Henan University, Kaifeng 475004, PR China (X. Wang). Institute of Atomic Manufacturing, Beihang University, Beijing 100191, PR China (C. Pan).
*E-mail addresses:* Wang, X. (xwang06@ahau.edu.cn), Pan, C. (pancaofeng@buaa.edu.cn).

 https://doi.org/10.1016/j.mattod.2024.08.001 

fulfill the unaddressed needs in the current field of sensory technology [2]. Human-like tactile sensors have garnered significant interest due to their potential applications in smart robots, which, with enhanced sensory capabilities, could broaden their utility in interactive tasks [3,4]. Over recent years, substantial efforts have been focused on advancing the development of tactile sensors [5–8]. A variety of tactile sensors have been developed by utilizing diverse transduction mechanisms, such as resistive [9–11], capacitive [12–16], piezoelectric [17], and triboelectric [18–21] types, which can convert mechanical stimuli into electrical signals. However, the effectiveness of single-modal tactile sensors that only produce electrical outputs is compromised by the issues such as crosstalk and noise, which prevents robots from interacting with the external environment as precisely and efficiently as humans do.

One notable advantage of the human sensory system is its ability to achieve more reliable perception through the analysis of multiple cues compared to relying solely on a unimodal cue. For instance, during interactions with the environment, humans can simultaneously receive and process both visual and haptic cues. These cues are intricately linked and interpreted in the inferior parietal cortex of humans, which enhances supramodal spatial abilities [22,23]. Such abilities enable humans to effectively navigate and avoid misjudgments caused by the environmental complexities, such as variations in an object's orientation. Developing multimodal tactile sensors, which are capable of simultaneously generating and analyzing multiple types of sensory information, will significantly improve the interactive capabilities of intelligent robots [24,25].

Among the signals directly perceived by humans, such as visible light, sound, and force, visible light is often considered the most suitable for interactive processes in human–machine interfaces (HMI) due to its higher spatial resolution and intuitiveness [26]. Mechanoluminescence (ML) has been integrated into tactile sensors to provide intuitive optical feedback of applied pressure [27–32]. However, while the ML can visualize the stress distribution in response to mechanical stimuli, its pressure threshold of several MPa is significantly higher than the gentle touch of human hands (typically less than 100 kPa). This high threshold severely limits its applicability in various user-interaction scenarios. In contrast, triboelectrification-induced electroluminescence (TIEL), which combines triboelectrification and electroluminescence (EL), offers several advantageous properties, including a low-pressure threshold, high brightness, and rapid response [26,33–37]. For example, the pressure threshold for TIEL is less than 10 kPa, which is three orders of magnitude lower than that of ML. Utilizing this low threshold, an advanced electronic signature system has been developed by analyzing consecutive frames from TIEL videos [34].

However, a detection threshold of 10 kPa is still insufficient for sensing subtle pressures. To address this, our group has developed a TIEL skin that can achieve high brightness and high-resolution for real-time imaging and HMI applications [38], where a pressure detection threshold as low as 1.2 kPa has been achieved. Moreover, the brightness of TIEL is 2.5 times stronger than that of an LED driven by a 2 V power supply. Despite these advancements, the brightness of TIEL remains insufficient for visibility in sunlight, limiting its use during daylight hours. Additionally, leveraging the rapid response of TIEL, a programmable optical-electrical dual-mode HMI system was developed for remote control applications [39]. However, its back electrode, containing only four separate channels within an area of 9 $cm^2$, offers low resolution and fails to achieve precise positioning. Hence, there is a critical need to develop a self-powered bimodal tactile imaging device (TID) that offers ultrasensitive pressure detection and precise positioning to accommodate the rapidly evolving demands of tactile sensing technologies.

In this study, we proposed a self-powered TID incorporating a high-dielectric thin film composed of $BaTiO_3$:La (BTO:La)/ZnS:Cu/polyvinylidene-fluoride-co-hexafluoropropylene(PVDF-HFP) (BLZP), which was coated on an array of laser-induced graphene (LIG) electrodes. After embedding BTO:La nanoparticles (NPs) into the PVDF-HFP matrix, a substantial increase in the dielectric constant of the BLZP film was achieved from 7.92 to 36.91. This modification significantly enhanced the luminescence brightness and enabled ultrasensitive pressure sensing ability. After optimizing the La concentration in the BTO:La and the content of BTO:La NPs in the PVDF-HFP matrix, the TIEL intensity of the BLZP film increased by 3.4 times compared to the ZnS:Cu/PVDF-HFP film without BTO:La NPs. Remarkably, the TIEL activated by an ultralow pressure of 1.0 Pa was observable in dark room. Compared to the ML, the TIEL of the BLZP film demonstrated superior stability, repeatability, and durability, thanks to its non-destructive light triggering mode and low-pressure threshold. The TIEL intensity remained consistent after 10,000 cycles of repeated friction at 10 kPa. The exceptional optical properties of the TIEL based on the BLZP film ensured visibility even under sunlight, exhibiting an impressive brightness. By recording the TIEL trajectories and stacking the TIEL images, the real-time visualization and recognition of handwritten letters was realized by these clear visible images with the aid of machine learning. To expand positioning dimensionality, the TID based on arrayed LIG electrodes successfully achieved precise touch position confirmation through tactile mapping based on output voltages generated by gentle tapping and sliding actions. Moreover, leveraging the optical-electrical bimodal tactile imaging capabilities of the TID, intelligent control was achieved through the synergistic effect of visualization recognition and precise touch positioning. Therefore, this work not only presents a new strategy for high-performance, tribo-induced, self-powered bimodal tactile imaging but also enhances intelligent human–machine interaction. This advancement is expected to broaden the potential applications of the TIDs in the fields of intelligent robotics, augmented reality, and human–machine interfaces (HMI).

## Results

### *Schematic illustration of the TID*

As schematically illustrated in Fig. 1a, the self-powered bimodal TID can simultaneously convert gentle touch stimuli into electrical and optical signals. When the finger slides on the surface of TID, the tribocharges are generated based on contact electrification, which will further induce a variational local electric field within the BLZP film to excite bright blue-green emission of ZnS:Cu phosphors and the corresponding electrical outputs of the bottom LIG electrodes. The induced blue-green emission as

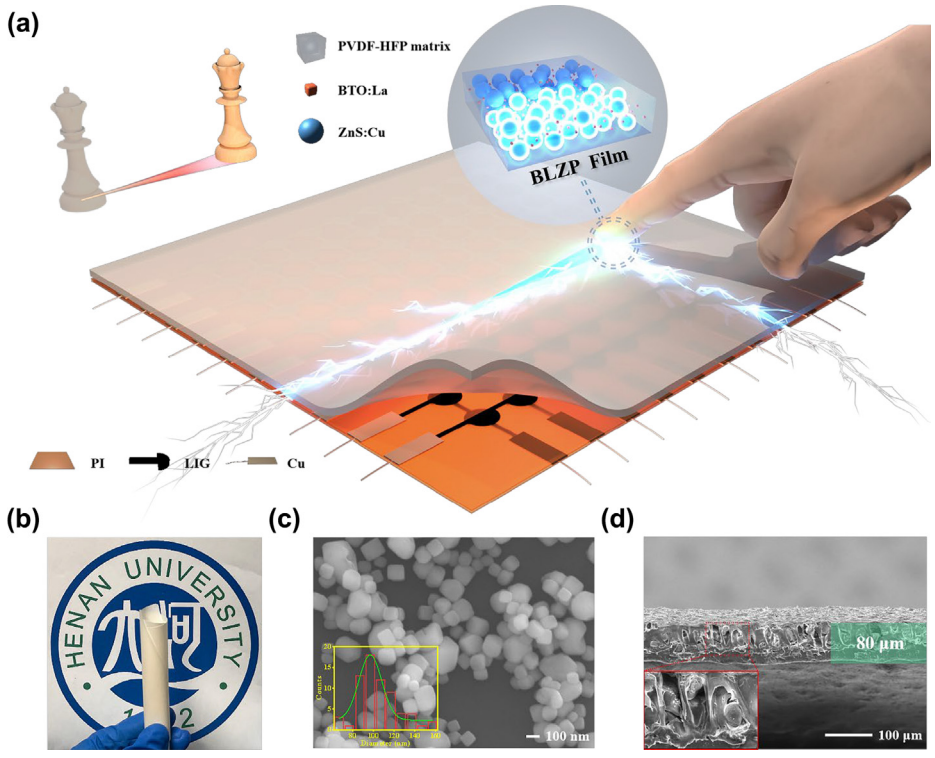


**FIG. 1**

**Self-Powered Bimodal TID.** (a) Schematic illustration of the TID capable of converting touch stimuli into both electrical and optical signals for intelligent control. (Inset: A detailed schematic of the BLZP film structure). (b) Digital photograph of the flexible BLZP film. (c) SEM image of the BTO:La nanoparticles (NPs) with an inset showing a histogram of the particle size distribution. (d) Cross-sectional SEM image of the BLZP film, demonstrating a uniform thickness of 80 μm.

an optical signal can be directly observed by naked eyes or captured by camera for visible tactile imaging. Simultaneously, the output voltage signals in the corresponding row and column electrodes can be recorded for precise positioning of finger sliding. Based on the optical-electrical bimodal tactile sensing, the self-powered bimodal TID will achieve ultrasensitive pressure sensing, real-time visualization recognition, and intelligent control. The TID is composed of high dielectric BLZP thin film coated on the arrayed LIG electrodes. As shown in the Inset of Fig. 1a, the BLZP thin film was formed through simultaneous embedding of BTO:La NPs and ZnS:Cu phosphors into the PVDF-HFP polymer matrix, which acted as both luminescence layer and friction layer. The detailed preparation procedures of BLZP film are presented in Fig. S1. Notably, the yielded BLZP film can be rolled up, as shown in Fig. 1b, which means the excellent flexibility of the BLZP film. As shown in Fig. 1c, scanning electron microscopy (SEM) image indicates a uniform cubic-shaped morphology and homogeneous distribution (100 nm average size) of BTO:La NPs. Moreover, energy dispersive spectroscopic (EDS) mapping exhibits uniform La, Ba, Ti and O elements distribution in BTO:La NPs without irrelevant elements (Fig. S2). As shown in Fig. S3, X-ray diffraction (XRD) pattern of the BTO:La NPs matches well with the standard ICDD card (05-0626) and reveals the high crystalline phase of BTO:La NPs without any by-products, such as Ba carbonate, which indicates the dopant La ions preferentially substitute Ba ions of $BaTiO_3$ (BTO) lattice due to similar ionic radii [40]. Additionally, a single (200) peak in the region near the 45-degree diffraction of XRD pattern was split into two specific (002) and (200) peaks after La doping, which could infer that the crystalline structure of BTO:La was transformed from cubic phase to tetragonal phase. To investigate the distribution and morphology of ZnS:Cu and BTO:La NPs within the PVDF-HFP matrix, the cross-sectional SEM images shown in Fig. 1d and Fig. S4 confirm that both ZnS:Cu and BTO:La NPs within the BLZP film still retain their original morphology (Fig. S4b and c). Furthermore, to verify the uniform distribution of ZnS:Cu and BTO:La NPs within the PVDF-HFP matrix, as shown in Fig. S5 and Fig. S6, respectively, both cross-sectional EDS image and surface EDS image of the BLZP film exhibit the uniform dispersions of Ba, Ti, O, La, Zn, S, Cu, and F elements from BTO:La NPs and ZnS:Cu throughout the PVDF-HFP matrix, indicating the embedded ZnS:Cu and BTO:La NPs are uniformly distributed within the PVDF-HFP matrix. The XRD pattern (Fig. S7) of BLZP film further proves that both ZnS:Cu phosphors and BTO:La NPs are embedded into PVDF-HFP matrix. Fig. S8 shows the ZnS:Cu phosphors with an average size of 16 μm. The XRD pattern of the ZnS:Cu phosphors is illustrated in Fig. S9, in which three major peaks of 28.72°, 46.67°, and 56.51° at $2\theta$ values corresponding to (111), (220), and (311) lattice planes, respectively, indicates a wurtzite structure of ZnS with perfect crystallinity.

### *Optical properties of the BLZP film*

The obtained blue-green TIEL emission with a peak at 498 nm is mainly contributed to the luminescence characters of ZnS:Cu phosphors in the BLZP film, as shown in Fig. S10 [41]. The TIEL

performances of the BLZP film is a result of the coupling of triboelectrification and EL, as illustrated in Fig. S11. The BLZP film serves as a positive triboelectric material, while polytetrafluoroethylene (PTFE) film acts as the negative counterpart. Initially, upon contact between the PTFE film and the BLZP film, an equal amount of negative and positive charges is generated on their respective surfaces. After continuous friction, the charges on both films gradually increase until a saturation state (Fig. S11-i). Subsequently, when the PTFE film slides away from the region containing ZnS:Cu phosphors (Fig. S11-ii), a strong local electric field is instantaneously established around the ZnS:Cu phosphors within the BLZP film, which leads to a bend in the energy band of ZnS lattice that prompts the detrapping of electrons trapped in shallow donor level and enables them to become free electrons within the conduction band [41]. The free electrons are then accelerated by the local electric field to move toward the top of the ZnS:Cu phosphors, at which point they possess enough kinetic energy to excite the luminescence centers of ZnS:Cu phosphors for light emission through impact excitation [42]. When the PTFE slides out of the BLZP film (Fig. S11-iii), the electrons are all concentrated at the top of the ZnS:Cu phosphors by the strong electric field, and no light emission occurs due to no interaction between the moving electrons and the luminescence centers. When the PTFE slides backward, the electrons at the top of the ZnS:Cu phosphors will move in reverse and impact with the luminescence centers, causing light emission again, as shown in Fig. S11-iv. Moreover, a test platform was set up to quantitatively characterize the optical properties of TIEL, as illustrated in Fig. S12, in which the PTFE film driven by a linear motor slid on the surface of the BLZP film. Simultaneously, an optic-fiber probe was fixed beneath the BLZP film to collect the light emission via the spectrometer, and a force sensor was affixed atop the sliding object to monitor vertical force on the contact surface. With dynamic interaction between the sliding object and the BLZP film, the bright blue-green TIEL can be recorded. Additionally, to investigate the influence of the ML on the TIEL, when a vertical pressure (over 20 N) was exerted on the BLZP film through a square PTFE film (20 × 20 $mm^2$), no light emission was observed from the BLZP film, as shown in Fig. S13, which indicates the ML of the BLZP film would be negligible.

To optimize the TIEL properties, the corresponding emission spectra have been investigated through various variables, including the ZnS:Cu content and BTO:La NPs content in the PVDF-HFP matrix, La molar ratio in BTO:La, material selection for the sliding object, sliding frequency, and the pressure at the contact surface (Fig. 2). It was found that the ZnS:Cu content in the ZnS:Cu/PVDF-HFP film played a crucial role in determining the TIEL properties. As shown in Fig. S14, the TIEL intensity increased with an increase of ZnS:Cu content from 41 to 50 wt% in the ZnS:Cu/PVDF-HFP film, and reached a maximum value at the weight ratio of 50 wt%. However, excessive ZnS:Cu would reduce the light emission due to the weakened contact electrification. Various types of materials as sliding objects were selected to achieve maximum contact electrification. It was found that PTFE as the sliding object could achieve synchronously the optimal TIEL and electrical voltage output (open-circuit voltage ($V_{OC}$)) based on freestanding-mode triboelectric nanogenerator (TENG), as illustrated in Figs. S15–S17. Moreover, the increase in PTFE sliding frequency from 13.3 to 93.3 Hz leaded to a monotonic enhancement of TIEL intensity (Fig. S18) due to more moving cycles of electrons in ZnS:Cu phosphors within a unit time interval to excite luminescence centers more frequently.

To further enhance the TIEL, high-dielectric BTO and BTO:La NPs have been embedded into ZnS:Cu/PVDF-HFP film, respectively. The content of BTO NPs should be firstly optimized. As shown in Fig. 2a, the intensity of TIEL based on BTO/ZnS:Cu/PVDF-HFP (BZP) film exhibits an increase with increasing the content of BTO in the BZP film from 0 to 1.7 wt%, while the TIEL intensity gradually decreases with a further increase of BTO (over 1.7 wt%), where the effective friction area of the PVDF-HFP may be reduced by the accumulation of BTO NPs on the BZP film. To intuitively demonstrate the enhancement of TIEL, the "e"-patterned light imaging also displayed similar enhancement as the TIEL intensity when an "e"-patterned PTFE film slid on the BZP film, as shown in Fig. 2b. Similarly, the electrical output ($V_{OC}$) of BZP films exhibited a consistent change trend with the TIEL, as shown in Fig. 2c, which indicated that the TIEL was closely related with triboelectrification effects. Furthermore, as a well-known grain growth inhibitor, the doped lanthanum (La) ions can dramatically adjust the dielectric properties of BTO [43]. Based on the optimal content of BTO (1.7 wt%) in the BZP film, the influence of La dopant concentration (0–1.5 mol %) in the BTO:La NPs on the TIEL performances of BLZP films has been further investigated. The TIEL spectra of BLZP films embedded by BTO:La with various La doping concentrations (0–1.5 mol%) are presented in Fig. 2d. Notably, as shown in Fig. 2e, when the La dopant concentration in the BTO:La NPs is 0.7 mol%, the maximum TIEL is achieved. Moreover, after embedding BTO:La (0.7 mol%), the integrated TIEL intensity of BLZP film (Fig. S19) is higher by 3.4 folds than that of ZnS:Cu/PVDF-HFP film without BTO:La NPs. Similarly, the $V_{OC}$ of the BLZP film reached 466 V at the optimal La dopant concentration of 0.7 mol% (Fig. 2f). In addition, the weak TIEL can be also observed under the repeated contact-separation of PTFE film with the BLZP film. Owing to low alternating output voltage of only about 10 V (Fig. S20a) under the contact-separation (1.5 Hz) in comparison with the sliding friction (over 400 V), the TIEL is mainly attributed to the sliding friction of the PTFE film on the BLZP film (Fig. S20b). The higher the triboelectrification-based output voltage ($V_{oc}$) is, the brighter the TIEL is. Moreover, the voltage-dependent brightness behavior can be modeled with Eq. (1) [42,44,45]

$$L = A\exp\left[\left(-\frac{B}{V^{\frac{1}{2}}}\right)\right] \quad (1)$$

where $L$ is the luminance, $V$ presents the applied voltage, $A$ and $B$ are constants determined by the particle size, the concentration of the phosphor powder in the dielectric, the dielectric constant of the embedding medium, and the device thickness. Notably, the applied voltage is a significant parameter to enhance the TIEL performances. Therefore, the embedding of BTO:La NPs into the BLZP film is proved to be a extremely effective strategy to enhance the TIEL performances.

Furthermore, the trigger pressure would bring out a significant influence on the TIEL properties. As shown in Fig. 2g, the TIEL intensity of BLZP film sharply increases with an increase of the

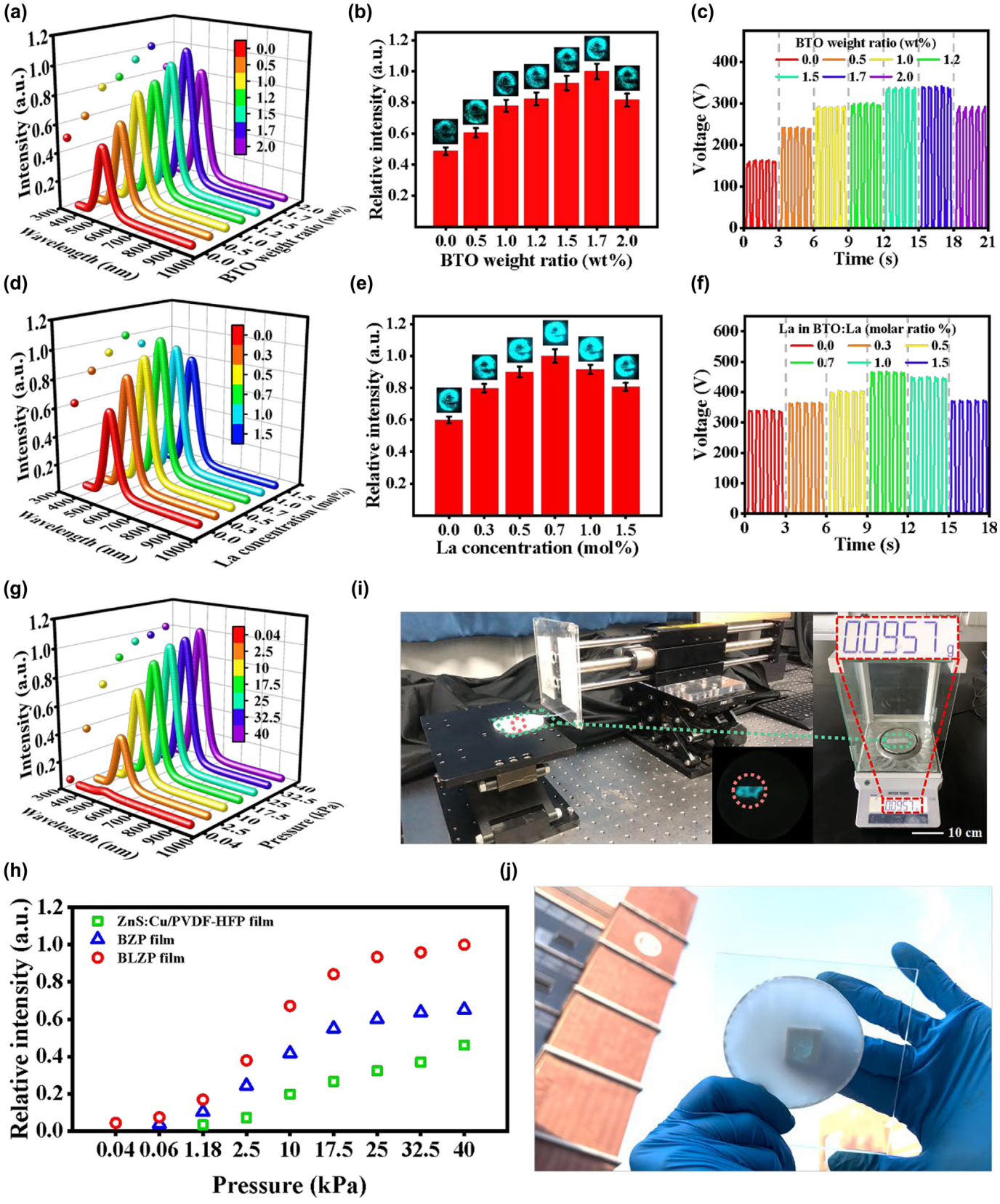


**FIG. 2**

**TIEL properties of BLZP film.** (a) TIEL spectra, (b) Relative integrated TIEL intensities, (c) $V_{OC}$ of the BZP films with various BTO weight ratios. (d) TIEL spectra, (e) Relative integrated TIEL intensities, (f) $V_{OC}$ of the BLZP films (1.7 wt% BTO:La with various La doping concentrations (0–1.5 mol%)). (g) TIEL spectra corresponding to an increase in applied pressure from 0.04 to 40 kPa. (h) Relative integrated TIEL intensities of three film types (ZnS:Cu/PVDF-HFP, BZP, and BLZP) as pressure increases from 0.04 to 40 kPa. (i) Ultrasensitive pressure detection (1.0 Pa) demonstrated by the TIEL. (j) High-brightness TIEL in sunlight, which is visible to the naked eyes.

trigger pressure from 0.04 to 40 kPa, and then reaches saturation over 40 kPa owing to the saturated tribocharge density. The pressure sensitivity of the TIEL of the BLZP film is defined as $\Delta I/\Delta P$, where $\Delta I$ is luminescence intensity variation and $\Delta P$ is pressure increment. To calculate the pressure sensitivity, the TIEL intensity was measured as an increase of the pressure. Their fitted curves can be divided into two regions, as shown in Fig. S21, where the sensitivity is 0.041 $kPa^{-1}$ in Region I (0.04–12.5 kPa) and 0.006 $kPa^{-1}$ in Region II (12.5–40 kPa). As illustrated in Fig. 2h, under the same pressure, the TIEL of BLZP film is brightest compared with the BZP and ZnS:Cu/PVDF-HFP films. Within the detection capability of our compact fiber spectrometer, a trigger pressure threshold of the BLZP film to generate the TIEL is 0.04 kPa, which is less than that of the BZP (0.06 kPa) and ZnS:Cu/PVDF-HFP (1.18 kPa) films. More importantly, the bright TIEL in the dark room can be easily observed by naked eyes under the gentle pressure (1.0 Pa) excitation when a low-weight PTFE film (0.0957 g, 2.0 × 5.0 $cm^2$, and 50 μm in thickness) as friction object sliding gently on the surface of the BLZP film, as shown in Fig. 2i, Fig. S22 and Movie S1 (Supplementary Information). To our knowledge, the ultralow pressure sensing of 1.0 Pa by the TIEL is the minimum detection threshold in comparison with the reported results, as depicted in Table S1 (Supplementary Information). To further demonstrate the superior brightness, the TIEL emission of the BLZP film in the sunlight is even visible to the naked eyes, as shown in Fig. 2j and Movie S2 (Supplementary Information). In addition, after the BLZP film was subjected to 10, 000 repeated frictions (10 kPa), its TIEL demonstrated excellent repeatability, stability, and durability, as shown in Fig. S23. The slight decrease in the intensity of TIEL is mainly attributed to the applied pressure fluctuations induced by the linear motor. Therefore, the BTO:La-embedded BLZP film can achieve ultrasensitive pressure sensing of 1.0 Pa, as well as an excellent bright TIEL emission with high repeatability and stability.

### *Dielectric effect on the TIEL properties*

To elaborate the effect of the embedding of BTO:La NPs into BLZP film on boosting the TIEL properties, Kelvin probe force microscopy (KPFM) technique was employed to examine the surface potential of the ZnS:Cu/PVDF-HFP, BZP, and BLZP film, respectively. The KPFM results showed the negative surface potential distribution on the surface of the ZnS:Cu/PVDF-HFP, BZP, and BLZP films without the sliding of PTFE. After charge injection by the sliding of PTFE, the reverse surface potential distribution on their surfaces was examined (Fig. 3a), indicating the electron transfer to the PTFE *via* electron tunneling. More importantly, as shown in Fig. 3b, the surface potential difference of the BLZP film was calculated to be +4.69 V, which is larger than that of ZnS:Cu/PVDF-HFP (+0.92 V) and BZP (+4.03 V) films, indicating a large amount of charge transfer between the PTFE and the BLZP films. The embedding of BTO:La NPs remarkably increased the surface potential difference of the BLZP film. Furthermore, the dielectric constant of BLZP film was measured at different alternating current (AC) frequencies, as presented in Fig. 3c, where the dielectric constant decreased with an increase of frequency from 10 kHz. It is found that the superior relative dielectric constant ($\varepsilon_r$) of the BLZP film is 36.91 at 10 kHz, which is 4.7-, 1.7-fold higher than that of ZnS:Cu/PVDF-HFP ($\varepsilon_r$ = 7.92) and BZP ($\varepsilon_r$ = 22.2) films, respectively. The influence of different component content on relative dielectric constant was further examined. As presented in Fig. S24a, the relative dielectric constant of BZP film increases with an increase of embedded BTO NPs in the BZP film and reaches a maximum value of 22.2 at 1.7 wt% BTO content. Nevertheless, further addition of BTO NPs (over 1.7 wt%) reduces gradually the relative dielectric constant of BZP film due to an increase of leakage current in the BZP film. To further increase the relative dielectric constant, the substitution of pure BTO NPs with the BTO:La NPs (1.7 wt %) led to a significant increase in the relative dielectric constant of BLZP film. The maximum value reaches 36.91 when the La molar concentration in the BTO:La NPs is 0.7 mol%, as depicted in Fig. S24b. The embedding of BTO:La NPs into the BLZP film contributes to the increase of its relative dielectric constant ($\varepsilon_r$ = 36.91). In the BTO:La NPs, the La ions preferentially substitute the Ba ions due to similar ionic radii, which induces a charge imbalance in the BTO lattice. Meanwhile, the Ti vacancies are generated to compensate the induced charge imbalance, which leads to the distortion of Ti-O bonding to generate local polarization that can increase the dielectric constant of BTO:La [46]. When the La concentration further increases from 0.7 mol% to 1.5 mol%, the dielectric property of BLZP film tardily declines, which is possibly attributed to the transformation of tetragonal BTO:La to cubic one [47]. The dielectric constant depicts the polarization capability of the dielectric materials under an external electric field, whose relationship can be expressed by the formula $P = (\varepsilon_r - 1)\varepsilon_0 E$. With an increase of the dielectric constant of the film, the degree of polarization becomes more pronounced, meaning that the electric polarization can be enhanced through increasing the dielectric constant of the film. Under the triboelectrification, the coupling of surface polarization of the PVDF-HFP and hysteresis dielectric polarization of BTO:La can enhance the charge transfer between the PTFE and the PVDF-HFP to increase the tribocharge density of the high-dielectric BLZP film [48].

The luminescence mechanism of TIEL is similar to that of high-field powder-like AC-driven EL based on the excitation mechanism by the hot-electron impact. The hot-electron impact excitation mechanism can be described as follows: (1) the electrons are injected and emitted from the interface states between the phosphor layer and dielectric layer as driven by high-AC electric field; (2) light is emitted by the donor-acceptor (D-A) recombination between the holes in the acceptor level ($Cu_{Zn}$) and the electrons captured in the shallow donor level (*Vs*) after impact excitation or impact ionization occurs between the accelerated electrons by frequent AC voltage and the luminescence centers of impurity ions in the host ZnS [45]. According to the hot-electron impact excitation mechanism involving inorganic phosphor materials, various factors, including device configuration and driving voltage, play important roles in determining the performance of EL devices [42]. Based on Gauss's theorem ($E = \sigma/(\varepsilon_0\varepsilon_r)$), the electric field strength is in inverse proportion to the relative dielectric constants, which renders most of electric field to focus on the ZnS:Cu phosphor in comparison with the BTO:La NPs in the BLZP film, as illustrated in Fig. S25. Furthermore, a simplified theoretical model was devised to realize two-

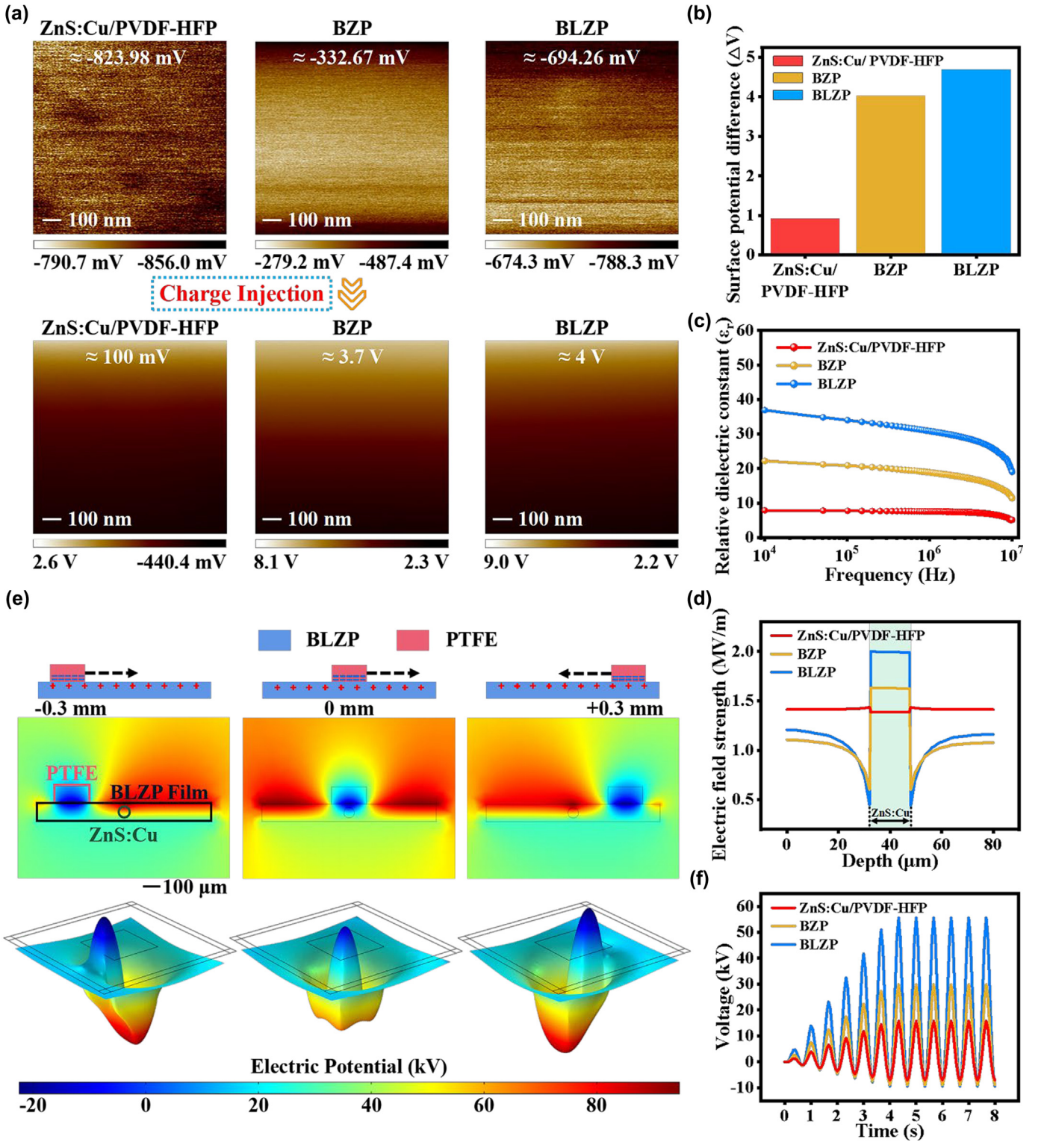


**FIG. 3**

**Dielectric effect on the TIEL performances.** (a) Surface potential for ZnS:Cu/PVDF-HFP, BZP, and BLZP films before and after charge injection. (b) A summarized histogram illustrating the difference in surface potential before and after charge injection. (c) The relative dielectric constant ($\varepsilon_r$) across varying frequencies. (d) The FEA of local electric field strengths along the depth of three films, differentiated by the relative dielectric constants of their matrices ($\varepsilon_2$). (e) Variations in electric potential distribution across the cross-section and surface of the BLZP film, triggered by the friction against a PTFE film (scale bar: 100 μm). (f) FEA depicting the oscillation of electric potential at the central point of ZnS:Cu, induced by the friction of PTFE film on the surface of the BLZP film.

dimensional electrostatics finite element analysis (FEA) via COMSOL Multiphysics, as depicted in Fig. S26. The detailed simulation is depicted in Supplementary Text. In this theoretical model, surface charge density is determined by the experimental measurement (398 μC/m$^{-2}$ in the BLZP, 219.5 μC/m$^{-2}$ in the BZP, and 120 μC/m$^{-2}$ in the ZnS:Cu/PVDF-HFP), as shown in Fig. S27. The simulation results exhibited that when the high-permittivity BTO:La was embedded in the BLZP film, the electric field strength across the ZnS:Cu phosphors was extremely enhanced owing to the great disparity in dielectric constants between the ZnS:Cu and the BTO:La NPs, meaning that the electric field was "concentrated" on the ZnS:Cu phosphors, as shown in Fig. 3d. The resulted local electric field strength can be calculated for the spherical ZnS:Cu phosphors with relative dielectric constant ($\varepsilon_1$ = 8.2) in the matrix with the relative dielectric constant ($\varepsilon_2$) according to the Equation:

$$E_{ZnS:Cu} = \frac{\sigma}{\varepsilon_0 \varepsilon_r}\left[\frac{3\varepsilon_2}{2\varepsilon_2 + \varepsilon_1 - \phi(\varepsilon_1 - \varepsilon_2)}\right] \quad (2)$$

where $\sigma$ denotes the surface charge density, $\phi$ is the volume fraction of the ZnS:Cu. The detailed derivation process of the electric field strength is depicted in Supplementary Text. For the BLZP film (thickness of 80 μm, surface charge density of 398 μC/m$^{-2}$, and $\varepsilon_2 \approx \varepsilon_r$ = 36.91), under the synergistic effect of enhanced surface charge density and focused electric field, the electric field strength based on Eq. (2) was calculated to be the order of $10^6$ V/m, consistent with the simulation results.

Additionally, the driving voltage with alternating features is crucial to accelerate persistently free electrons to excite luminescence centers for light emission through impact excitation within ZnS:Cu phosphors, resulting in the reliable and stable TIEL with high light emission properties. To further investigate the alternating features of driving voltage converted from triboelectrification between the PTFE and BLZP films, we conducted electrostatics FEA to analyze the variations in electric field and electric potential on the cross section and surface of the BLZP film during the friction process of PTFE film. Initially, there exists no induced electric field and electric potential around the BLZP film due to no tribocharges between the PTFE and the BLZP film. Subsequently, with the sliding of the PTFE on the BLZP films, equal amount of opposite tribocharges continuously accumulate on their surfaces to induce the electric field and electric potential. After the tribocharges reach saturation, periodic variations in the electric field and electric potential follow the sliding of PTFE. During the process of tribocharge accumulations, the changes in the electric field across the cross-section of the BLZP film and the variations in the surface potential distribution of the BLZP film are displayed in Movie S3 and Movie S4, respectively. After their tribocharges reach saturation, the 2D electric potential distribution variation across the BLZP film is further illustrated in the top of Fig. 3e following the motion of PTFE, as well as the 3D electric potential distribution variation on the surface of BLZP film (in the bottom of Fig. 3e). During the negatively charged PTFE sliding across the surface of the BLZP film, notable electric potential variation occurs around the ZnS:Cu phosphor in the BLZP film, which is mainly attributed to the significant variations in surface electric potential distribution of the BLZP film. Based on the tribocharge accumulation model, both the electric field and electric potential in the center of ZnS:Cu phosphors were further analyzed, thus an oscillatory feature occurs to the electric field and electric potential from a progressive increase to a stable state, as shown in Fig. S28 and Fig. 3f, respectively. Significantly, the amplitudes of the simulated electric field and electric potential in the center of ZnS:Cu phosphor in the BLZP film are much larger than those in the BZP and ZnS:Cu/PVDF-HFP films, thereby the embedding of high dielectric BTO:La NPs plays a significantly important role in boosting the TIEL properties of the BLZP film.

### *Tactile imaging and real-time visualization recognition*

Inspired by ultrasensitive pressure sensing and superior brightness, the TIEL has been developed to achieve visible tactile imaging and accurate real-time visualization recognition under aid of machine learning, as illustrated in Fig. 4a. When handwriting the letters on the BLZP film, the TIEL can follow the handwriting trajectory and can be recorded by the camera to be a series of live images of consecutive frames. After stacking these separate frames together, an overall tactile image of the handwritten letter (such as "B") was observed on the screen, as shown in Movie S5 (Supplementary Information). It is obvious that the TIEL intensity varies along the handwriting trajectory owing to the variation of handwriting force and velocity during handwriting letters. To realize the quantification of the TIEL intensity of handwriting the letters, the stacked image is processed to be the quantitative mapping through grayscale image conversion (Fig. S29), as shown in Fig. 4c. Based on the quantitative mapping, a convolutional neural network (CNN) model of machine learning was employed to achieve accurate real-time visualization recognition of tactile images of handwritten letters. As illustrated in Fig. 4b, the CNN model consists of convolutional (Conv) layers, pooling (Pool) layers, rectified linear unit (ReLU) layers, and Softmax layer. The corresponding comprehensive information and parameters are summarized in Supplementary Text and Table S2, respectively. The CNN model executed feature extraction of tactile images through its convolution operation. For instance, 26 capital letters were repeatedly written for 50 times to establish a complete data set (1300 samples) for feature engineering, including data preprocessing, feature extraction, and feature selection. After feature engineering, the entire dataset was partitioned into a training set and a validation set with a corresponding ratio of 7:3. Subsequently, the relationship between the feature matrix and the labels was established by using a CNN model designed with TensorFlow, followed by continuous iterations. As depicted in Fig. 4d, when the number of training iterations increased, the CNN model gradually approached the true value. As a result, the recognition accuracy of ten different handwritten letters reached 100 % (Fig. 4e), indicating that the trained CNN model had a high positive predictive value and true positive rate for visualization recognition. Combining the tactile imaging with the trained CNN model, a real-time visualization recognition has been achieved through displaying timely recognition results of handwritten letters ("T, I, E, L"), as shown in Movie S6 (Supplementary Information), which will enable the feasibility of real-time HMI.

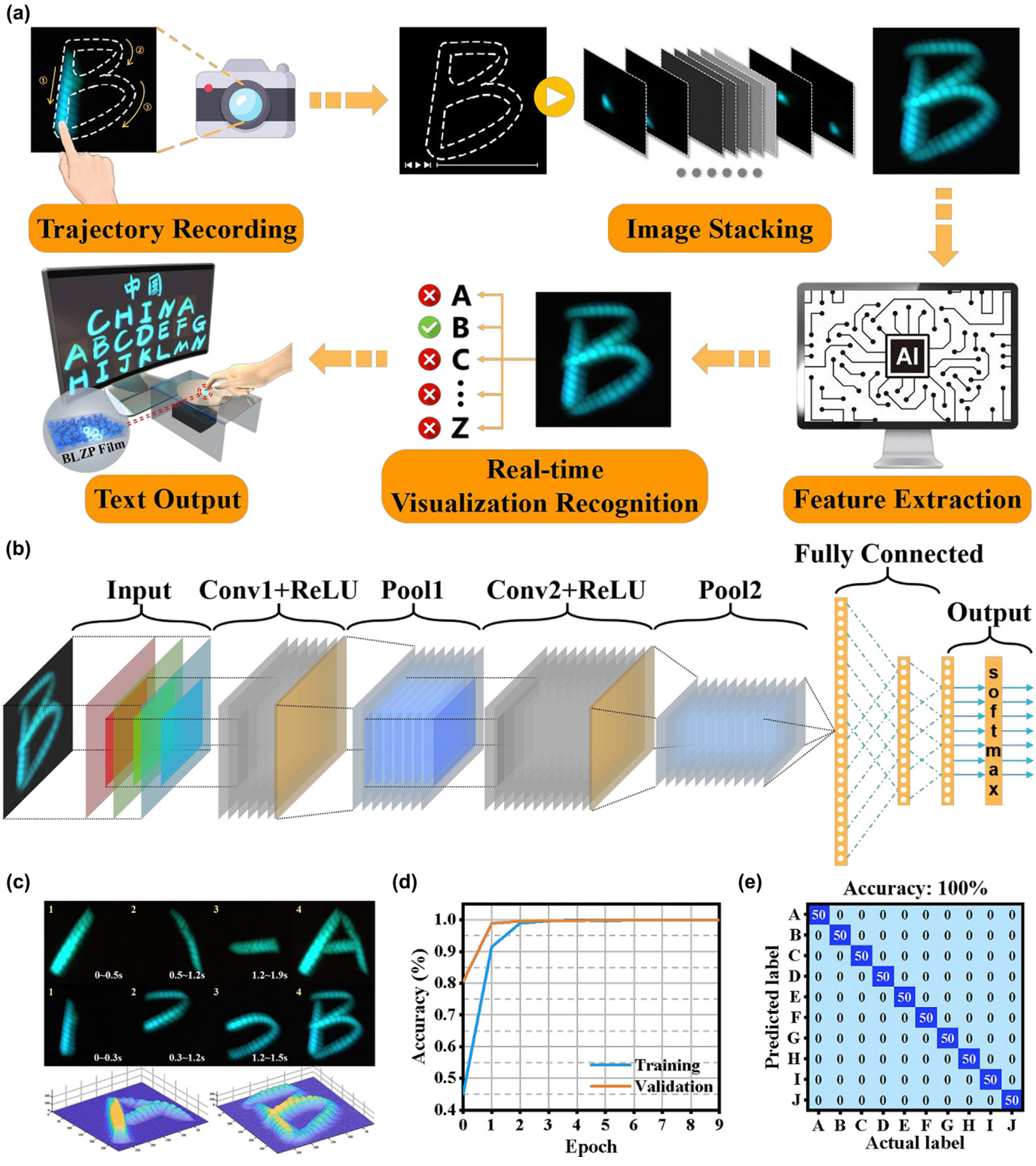


**FIG. 4**

**Tactile imaging and real-time visualization recognition.** (a) Flowchart illustrating the process of tactile imaging and real-time visualization recognition. (b) CNN model utilized for image recognition. (c) Tactile representations of handwritten letters displayed at the top, with quantitative intensity mapping provided at the bottom. (d) Graph showing the improvement in prediction accuracy of visualization recognition as the number of training epoch increases. (e) Confusion matrix demonstrating the visualization recognition with a perfect accuracy of 100%.

*Tactile mapping of the TID*

Precise positioning, as well as ultrasensitive pressure sensing, is extremely important for the HMI. To achieve simultaneously touch positioning and visible tactile imaging, as illustrated in Fig. 5a, the TID was developed based on arrayed TENG that was fabricated through the BLZP film as triboelectric layer coated on the row-column-crossing overlapping LIG electrodes according to our previous method (Fig. S30) [20]. The corresponding parameters of the arrayed LIG pattern are shown in Fig. S31. As displayed in Fig. 5b, the circle-shaped working electrodes were formed through complementary intersection overlapping between upper and lower aligned semicircular LIG electrode arrays. According to the coupling effect of contact electrification and electrostatic induction, the working principle of one array unit (Fig. 5b) in the TID, consistent with our previous work [20], is illustrated in Fig. S32. The arrayed TENG-based TID will achieve accurate touch position confirmation through mapping output voltages generated by gentle touching and sliding. The touch position confirmation is based on the cross-locating voltage signals of the row-column crossing overlapping TID. The

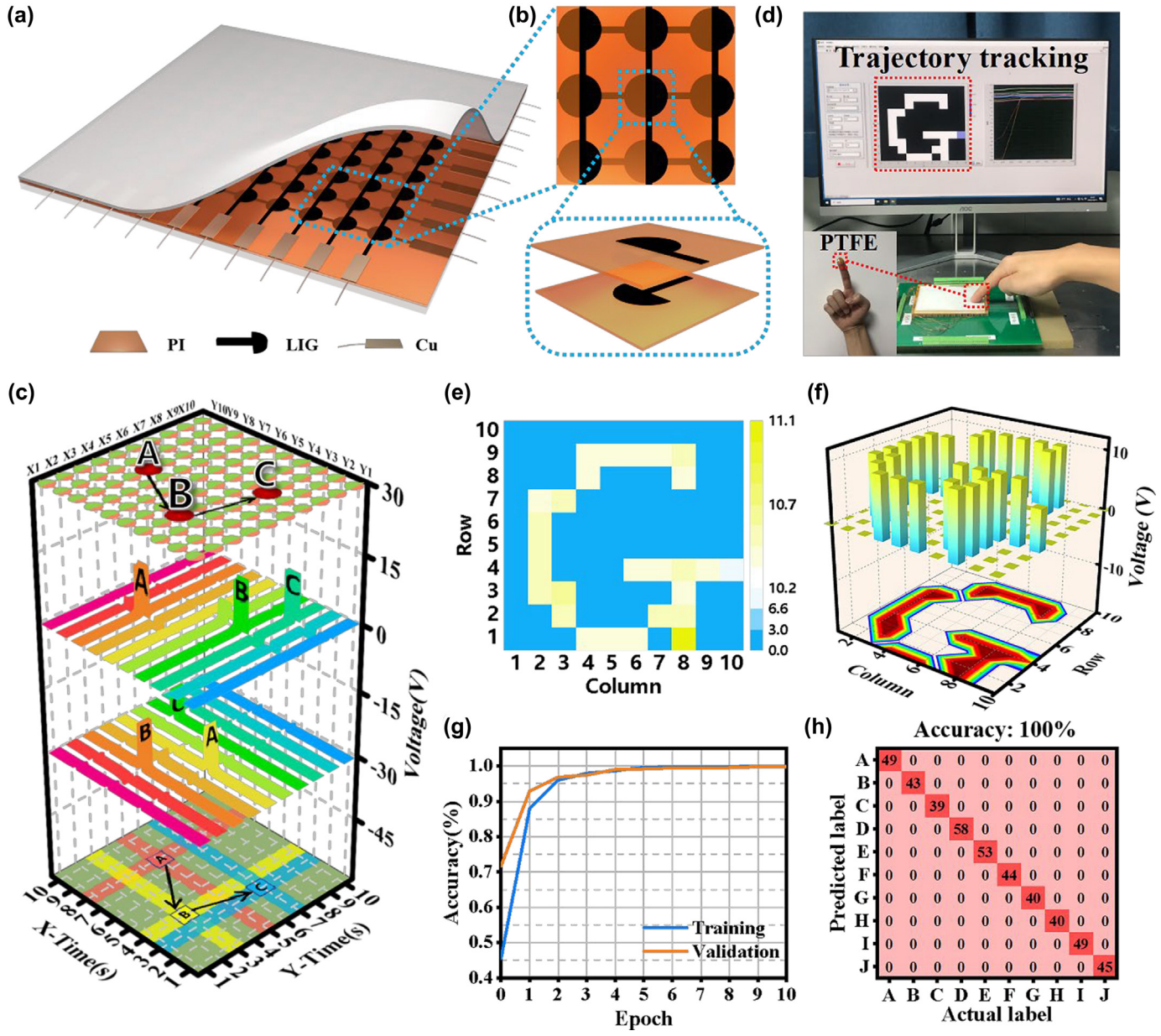


**FIG. 5**

**Tactile mapping based on output voltage.** (a) Schematic representation of a 10 × 10 pixelated TID. (b) Detailed enlarged top view illustrating the configuration of the TID and the pixel structure of a single sensor unit. (c) Voltage signals captured using a multichannel data acquisition card, accompanied by schematic descriptions of the data processing techniques used for tactile mapping through a cross-type arrayed laser-induced graphene (LIG) electrodes. (d) Trajectory tracking enabled by multichannel signal acquisition. (e) Top view displaying 2D mapping of output voltage intensity from the handwritten letter "G" on the surface of the TID. (f) Tactile mapping representation of the handwritten letter "G" in a 3D view. (g) Graph showing the increase in prediction accuracy for handwritten letter recognition as the number of training epoch progresses. (h) Confusion matrix illustrating the accuracy of handwritten letter recognition.

voltage signals can be collected from the corresponding row and column ports when a finger with PTFE touches one array unit. When the finger touches one coordinate ($X_i$, $Y_j$), the corresponding row $X_i$ and column $Y_j$ channels will generate voltage signals simultaneously, which can be recorded by the multichannel data acquisition card. It is easy to identify multipoint touching (such as A, B, and C) according to the voltage output of corresponding channels, such as ($X_5$, $Y_8$), ($X_3$, $Y_4$), and ($X_7$, $Y_3$), as shown in Fig. 5c. It is worth noting that because there exists a distinct differentiation between the signals and the noise, the TID will offer valid tactile mapping of output voltage. To demonstrate the capability of precise positioning of the TID, the trajectory of handwriting the letter ("G") can be tracked based on the mapping of real-time generated output voltage signals, which can be real-time displayed on the screen (Fig. 5d). The corresponding 2D touch mapping image of the handwritten letter "G" is shown in Fig. 5e. To further display the distinct contrast between the touched and untouched array units, the corresponding 3D touch mapping image is illustrated vividly in Fig. 5f, which highlights the effectiveness of tactile mapping based on the TID. Similarly, the CNN model of machine learning was also employed to process the tactile mapping images of handwritten letters (A–J) for the recognition. As illustrated in Fig. 5g, when the count of training iterations reached 10, both the training and validation set achieved an accuracy of 100 %. Fig. 5h exhibits a confusion matrix of the verifying results, demonstrating an average recognition accuracy of 100 % for 10 types of handwritten letters. The high accuracy indicates that the TID is capable of realizing precise touch position confirmation.

### *Intelligent control system based on the bimodal TID*

To demonstrate the synergetic effect of precise touch positioning and visualization recognition, an intelligent control system was established based on bimodal optical and electrical signals of the TID. As illustrated in Fig. 6a, the bimodal TID demonstrates high performances in precise touch positioning and visualization

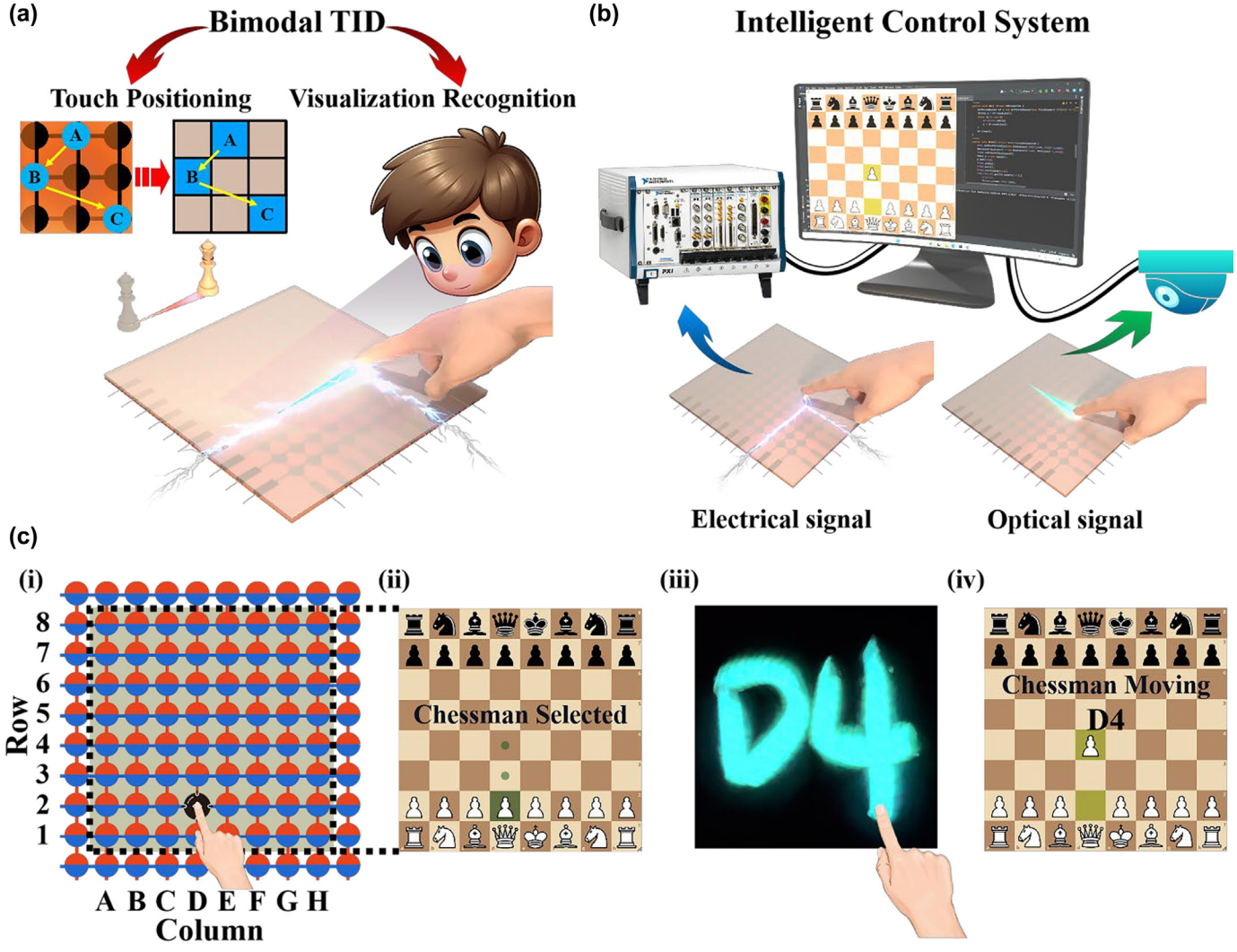


**FIG. 6**

**Intelligent control system based on the bimodal TID.** (a) Schematic diagram illustrating the bimodal functionality of the TID for touch positioning and visualization recognition. (b) Detailed schematic representation of the touch positioning module and visualization recognition module within the intelligent control system. (c) Schematic illustration depicting chessman manipulation as a proof-of-concept: (i) and (ii) Selection of chessmen achieved through touch positioning, utilizing the electrical signals from arrayed electrodes. (iii) and (iv) Movement of chessmen facilitated by visualization recognition, employing visible tactile imaging from TIEL signals.

recognition, where the touch positioning is realized through mapping the output voltages, while the visualization recognition is achieved by stacking the TIEL images. Based on the bimodal optical and electrical signals of the TID, an intelligent control system was established (Fig. 6b). In the touch positioning module, when the finger touches one coordinate ($X_i$, $Y_j$) of the TID, the corresponding generated electrical signals are recorded by the multichannel data acquisition card and then sent to the computer through Bluetooth. Subsequently, the electrical signals are encoded as touch positioning data that is stored in a designated path to be read by Java program. After touch positioning, the multichannel data acquisition card reverts to standby mode for subsequent instructions. In the visualization recognition module, when a finger handwrites on the surface of the TID, the optical signals based on the corresponding TIEL are recorded by a camera and then are utilized for real-time visualization recognition. The recognition results are saved in the designated path for eventual reading of Java program. To demonstrate the intelligent control ability of the TID, the virtual chessman as a proof-of-concept was successfully manipulated. As shown in Fig. 6c-i, the middle of the 8 × 8 electrode array was defined as the effective region for chessmen manipulation. When the finger touched the coordinate "D2", the white chessman in the corresponding position would be selected (Fig. 6c-ii). Subsequently, when handwriting down "D" and "4" on the surface of TID in turn (Fig. 6c-iii), the selected chessman would be moved to the coordinate of "D4" (Fig. 6c-iv)). Similarly, the black chessman selected by the touching in the coordinate "B8" will move to "C6" position following the handwriting of "C" and "6" on the TID surface. The detailed manipulation process of the virtual chessmen is shown in Movie S7 (Supplementary Information). In light of its intelligent control capability, the bimodal TID has effectively demonstrated its potential in assisting humans to execute complex machine manipulation, which means its promising prospects for intelligent control and HMI.

## Conclusion

In summary, this research has successfully demonstrated the self-powered, bimodal TID, composed of the high-dielectric BLZP film coated on the arrayed LIG electrodes, for ultrasensitive pressure sensing, real-time visualization recognition, touch position confirmation, and intelligent control. Under low trigger pressure threshold of 1.0 Pa, the TID can efficiently convert gentle touch stimuli into bright TIEL and electrical output without external power. Enhancements in the dielectric constant of the BLZP film significantly intensify the electric field focused on the underlying ZnS:Cu phosphors within the BLZP film, leading to a marked increase in the TIEL brightness and enabling ultrasensitive pressure detection. Leveraging its superior optical properties, the TID supports visible tactile imaging and precise real-time visualization recognition, assisted by machine learning. Additionally, the TID's arrayed TENG-based configuration allows for exact touch position confirmation via tactile mapping, triggered by gentle tapping and sliding. Importantly, an intelligent control system utilizing both optical and electrical signals from the TID has been implemented to showcase the synergistic integration of precise touch positioning and advanced visualization recognition. Consequently, this self-powered, bimodal TID represents a significant advancement in the fields of ultrasensitive pressure sensing, real-time visualization recognition, touch position confirmation, and intelligent control.

## CRediT authorship contribution statement

**Kangting Liu:** Writing – original draft, Visualization, Validation, Methodology, Investigation, Formal analysis, Data curation. **Yifan Xia:** Software, Methodology, Investigation. **Xinrong Zhi:** Validation, Software, Methodology, Investigation, Data curation. **Shuhan Li:** Validation, Software, Methodology, Investigation, Data curation. **Siyu Zhang:** Software, Methodology. **Biao Yang:** Software, Methodology. **Mingyuan Li:** Software, Methodology. **Xin Wang:** Writing – review & editing, Validation, Supervision, Resources, Project administration, Funding acquisition, Conceptualization. **Caofeng Pan:** Writing – review & editing, Conceptualization.

## Data availability

Data will be made available on request.

## Declaration of competing interest

The authors declare that they have no known competing financial interests or personal relationships that could have appeared to influence the work reported in this paper.

## Acknowledgements

The authors gratefully acknowledge financial support from National Natural Science Foundation of China (No. 11774384) and Natural Science Foundation of Henan (No. 232300421215).

## Appendix A. Supplementary material

Supplementary material to this article can be found online at https://doi.org/10.1016/j.mattod.2024.08.001.

### References

[1] C. Wan et al., Nat. Commun. 11 (2020) 4602. https://doi.org/10.1038/s41467-020-18375-y.
[2] Y. Zhao et al., Adv. Mater. 33 (2021) e2102332. https://doi.org/10.1002/adma.202102332.
[3] M.L. Hammock et al., Adv. Mater. 25 (2013) 5997. https://doi.org/10.1002/adma.201302240.
[4] Y. Guo et al., Adv. Mater. 35 (2023) e2300855. https://doi.org/10.1002/adma.202300855.
[5] S. Pyo et al., Adv. Mater. 33 (2021) e2005902. https://doi.org/10.1002/adma.202005902.
[6] Y. Li et al., InfoMat 5 (2023) e12463. https://doi.org/10.1002/inf2.12463.
[7] H. Niu et al., InfoMat 6 (2023) e12500. https://doi.org/10.1002/inf2.12500.
[8] K. Zhou et al., Nano Energy 70 (2020) 104546. https://doi.org/10.1016/j.nanoen.2020.104546.
[9] T. Yang et al., ACS Nano 15 (2021) 11555. https://doi.org/10.1021/acsnano.1c01606.
[10] K. Zhou et al., Small 17 (2021) e2100542. https://doi.org/10.1002/smll.202100542.
[11] H. Zhang et al., Nano Lett. 24 (2024) 4002. https://doi.org/10.1021/acs.nanolett.4c00623.
[12] N. Bai et al., Nat. Commun. 11 (2020) 209. https://doi.org/10.1038/s41467-019-14054-9.
[13] Y.J. Guo et al., Adv. Funct. Mater. 32 (2022) 2203585. https://doi.org/10.1002/adfm.202203585.
[14] X.Y. Lu et al., Adv. Mater. Technol. 8 (2023) 2202123. https://doi.org/10.1002/admt.202202123.

[15] Z. Shen et al., Adv. Mater. 33 (2021) e2102069. https://doi.org/10.1002/adma.202102069.
[16] J. Shi et al., Sci. Adv. 9 (2023) eadf8831. https://doi.org/10.1126/sciadv.adf8831.
[17] J. Zhong et al., ACS Nano 13 (2019) 7107. https://doi.org/10.1021/acsnano.9b02437.
[18] C.K. Qiu et al., IEEE Access 7 (2019) 92745. https://doi.org/10.1109/Access.2019.2927394.
[19] W.Y. Guo et al., Nano Energy 108 (2023) 108229. https://doi.org/10.1016/j.nanoen.2023.108229.
[20] Z. Yan et al., Adv. Funct. Mater. 31 (2021) 2100709. https://doi.org/10.1002/adfm.202100709.
[21] J. He et al., Adv. Funct. Mater. 32 (2021) 2107281. https://doi.org/10.1002/adfm.202107281.
[22] V. van Polanen, M. Davare, Neuropsychologia 79 (2015) 186. https://doi.org/10.1016/j.neuropsychologia.2015.07.010.
[23] E. Freud et al., Trends Cogn. Sci. 20 (2016) 773. https://doi.org/10.1016/j.tics.2016.08.003.
[24] X. Ma et al., ACS Nano 16 (2022) 2789. https://doi.org/10.1021/acsnano.1c09779.
[25] C. Wang et al., Adv. Intell. Syst. 1 (2019) 1900090. https://doi.org/10.1002/aisy.201900090.
[26] X. Zhao et al., Sci. Adv. 6 (2020) eaba4294. https://doi.org/10.1126/sciadv.aba4294.
[27] S.M. Jeong et al., Energy Environ. Sci. 7 (2014) 3338. https://doi.org/10.1039/c4ee01776e.
[28] S. Song et al., Mater. Today 32 (2020) 46. https://doi.org/10.1016/j.mattod.2019.08.004.
[29] F.L. Wang et al., Nano Energy 63 (2019) 103861. https://doi.org/10.1016/j.nanoen.2019.103861.
[30] X.D. Wang et al., Nano Energy 55 (2019) 389. https://doi.org/10.1016/j.nanoen.2018.11.014.
[31] X. Wang et al., Adv. Mater. 27 (2015) 2324. https://doi.org/10.1002/adma.201405826.
[32] P.F. Zhang et al., ACS Sustain. Chem. Eng. 11 (2023) 4073. https://doi.org/10.1021/acssuschemeng.2c05955.
[33] L. Su et al., J. Phys-Mater. 4 (2021) 042001. https://doi.org/10.1088/2515-7639/abfcab.
[34] X.Y. Wei et al., Adv. Mater. 28 (2016) 6656. https://doi.org/10.1002/adma.201600604.
[35] Y. Wang et al., ACS Appl. Mater. Interfaces 11 (2019) 13796. https://doi.org/10.1021/acsami.9b02313.
[36] X.J. Zhao et al., Nano Energy 75 (2020) 104823. https://doi.org/10.1016/j.nanoen.2020.104823.
[37] L. Su et al., Mater. Horizons 10 (2023) 2445. https://doi.org/10.1039/d3mh00172e.
[38] C. Jia et al., Adv. Funct. Mater. 32 (2022) 2201292. https://doi.org/10.1002/adfm.202201292.
[39] L. Su et al., Adv. Sci. 9 (2022) e2203510. https://doi.org/10.1002/advs.202203510.
[40] M. Ganguly et al., J. Alloy. Compd. 579 (2013) 473. https://doi.org/10.1016/j.jallcom.2013.06.104.
[41] J. Li et al., ACS Appl. Mater. Interfaces 14 (2022) 4775. https://doi.org/10.1021/acsami.1c23155.
[42] Z.L. Yang et al., Cell Rep. Phys. Sci. 1 (2020) 100213. https://doi.org/10.1016/j.xcrp.2020.100213.
[43] M.A. Gomes et al., J. Mater. Sci. 51 (2016) 4709. https://doi.org/10.1007/s10853-016-9789-7.
[44] R. Shanker et al., Adv. Funct. Mater. 29 (2019) 1904377. https://doi.org/10.1002/adfm.201904377.
[45] M. Bredol, H.S. Dieckhoff, Materials 3 (2010) 1353. https://doi.org/10.3390/ma3021353.
[46] S.P. Culver et al., Chem. Commun. 50 (2014) 3480. https://doi.org/10.1039/c3cc49575b.
[47] Y.P. Wang et al., Mater. Charact. 172 (2021) 110859. https://doi.org/10.1016/j.matchar.2020.110859.
[48] J. Wang et al., Nat. Commun. 8 (2017) 88. https://doi.org/10.1038/s41467-017-00131-4.